Hierarchical structure of Sb-doped monoclinic WO_3 towards NO_2 gas detection at low temperature†

Juanjuan Qi[a‡], Ke Chen [a‡], Yi Xing*[b], Hua Fan [a], Hewei Zhao [a], Jie Yang [a], Lidong Li*[a], Binyi Yan[c], Jing Zhou*[c], Lin Guo*[a], and Shihe Yang *[a,d]

[a] School of Chemistry, Beihang University, Beijing 100191, China
[b] School of Civil and Environmental Engineering, University of Science and Technology Beijing, Beijing, 100083, China
[c] College of Chemistry Engineering, Northeast Dianli University, Jilin 132012, P. R. China
[d] Department of Chemistry, The Hong Kong University of Science and Technology, Clear Water Bay, Kowloon, Hong Kong, China

Corresponding author. E-mail: guolin@buaa.edu.cn; xingyi@ustb.edu.cn; lilidong@buaa.edu.cn; zhoujing@mail.nedu.edu.cn; chsyang@ust.hk;

‡Juanjuan Qi and Ke Chen are equal to the contribution for this work.

Electronic Supplementary Information

Results and discussion

Table S1. The changes of bond length of M (metal) and O before and after Sb-doped in the WO_3 cell. (unit: Å)

Structure	+x	-x	+y	-y	+z	-z
WO_3	1.995	1.814	1.985	1.818	2.072	1.780
$Sb_xW_{1-x}O_3$	1.949	1.939	1.961	1.946	1.971	1.955
Δ	-0.046	0.125	-0.024	0.128	-0.101	0.175

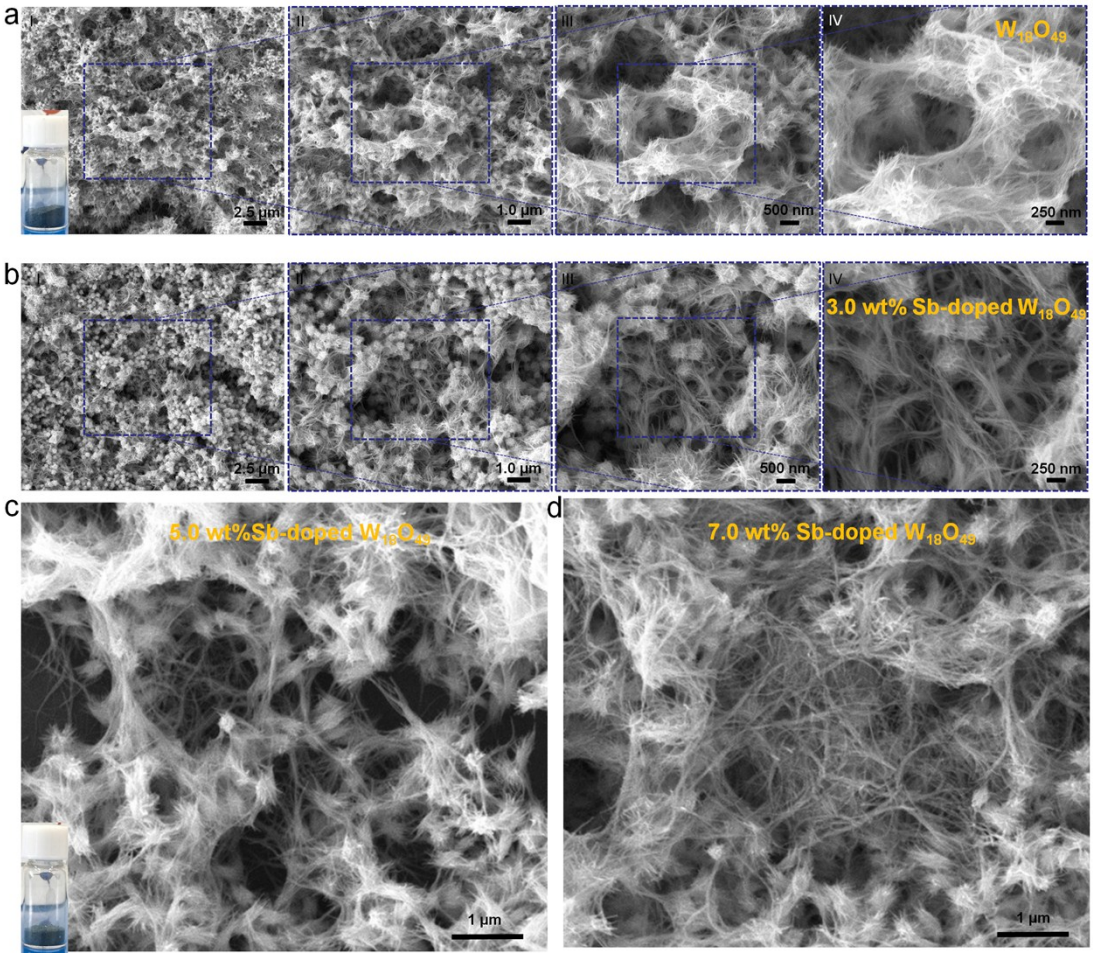

Fig. S1 ESEM images of multi-scaled morphologies for urchin-like nanocrystals with some nanowires prepared by the first-step solvothermal reaction. a) pure b-$W_{18}O_{49}$. Inset is a digital photo that shows a blue color of the sample. b) 3.0 wt%-Sb-doped $W_{18}O_{49}$. c) 5.0 wt% Sb-doped $W_{18}O_{49}$. Inset is a digital photo that shows a simialr blue color of the sample. d) 7.0 wt% Sb-doped $W_{18}O_{49}$. These results indicate that different amount dopants of Sb (e.g., 0-7 wt%) are introduced to the synthesis system and their morphologies are similar.

The scanning electron microscopy (SEM) image shows that the as-synthesized samples (Sb-doped $W_{18}O_{49}$) are an urchin-like hierarchical structure (Fig. S1). Sb-

doped $W_{18}O_{49}$ is a monoclinic type structure (*P*2/*m*), similar with pure $W_{18}O_{49}$.[1] Therefore, we can infer that the monoclinic Sb-doped $W_{18}O_{49}$ consists of an ordered 2D lattice of edge-sharing distorted Sb-doped WO_6 octahedra that form a network of pentagonal columns interspersed with hexagonal channelas.

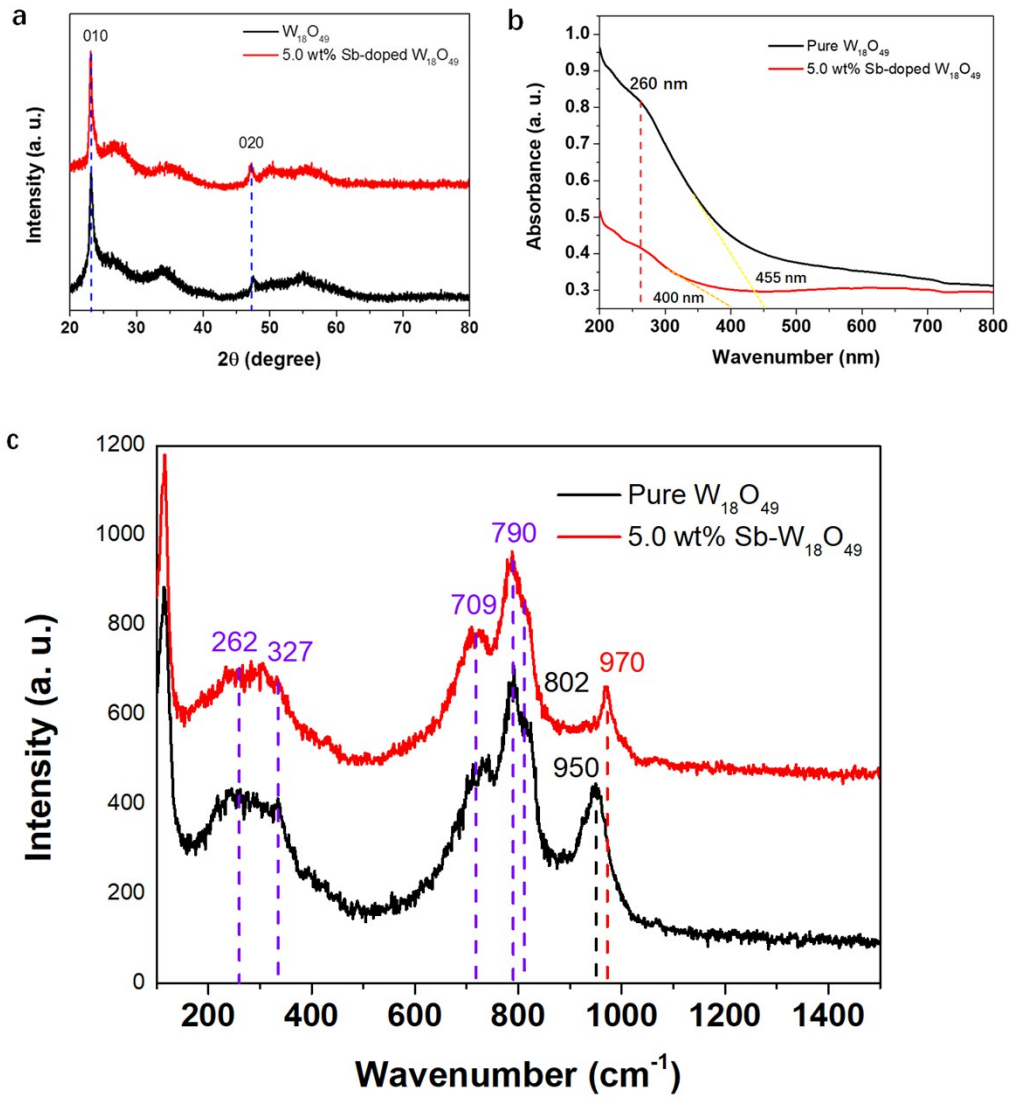

Fig. S2 Characterization curves for urchin-like nanocrystals ($W_{18}O_{49}$ and 5.0 wt% Sb-doped $W_{18}O_{49}$) with some nanowires prepared by the first-step solvothermal reaction. (a) The typical XRD pattern. (b) The UV-Visible spectra. (c) The Raman spectra.

The X-ray diffraction (XRD) pattern of our sample displays mainly two intense diffraction peaks, corresponding to the (010) and (020) crystal faces of the monoclinic $W_{18}O_{49}$ structure (JCPDS no.36-101),[2] as shown in Fig. S2a. All of the other diffraction peaks are much weaker, resulting in broad diffraction peak. The narrow (010) and (020) diffraction peaks stongly suggest that the possible crystal growth direction of the sample is [010], because the close-packed planes of the monoclinic $W_{18}O_{49}$ crystal are {010}.[3] Figure S2b show that the characteristic adsorption absorption edge shifted from about 455 nm in pure WO_3 to approximately 400 nm in Sb-doped WO_3, giving rise to the great blue shift of characteristic absorption band.

In the Raman spectrum (Fig. S2c), the O-W-O bending modes at 262 and 327 cm^{-1} in the low wavenumber region and W-O stretching modes at 709 and 802 cm^{-1} in the high wavenumber region were both observed, which is agreement with the characterstics of $W_{18}O_{49}$ previously reported.[4] After Sb doping treatment, the characteristic Raman band at 950 cm^{-1} (corresponding to O-W-O or W=O terminal vibration stretching mode) was found to shift towards higher wavenumber,[5] which may give an evidence that large amounts of structural defects are produced by the doping treatment.

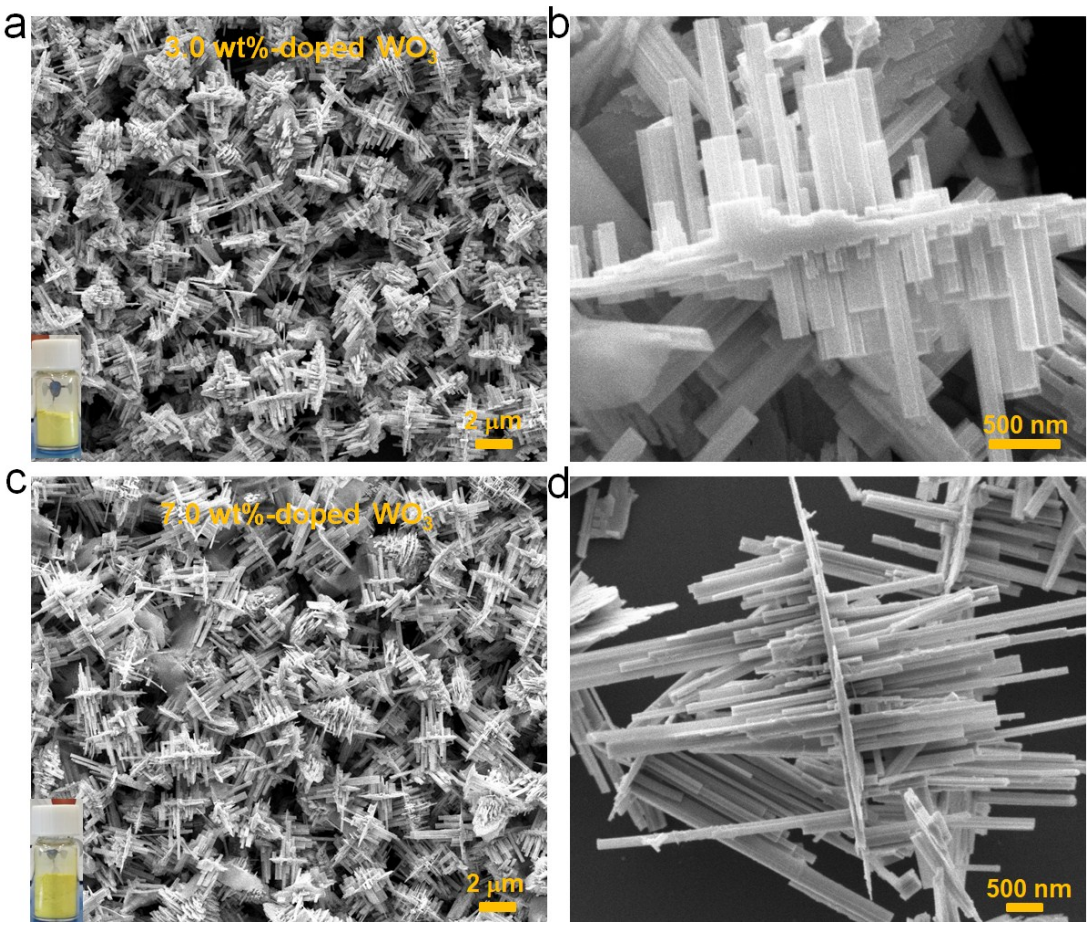

Fig. S3 ESEM images of the 3D HMSW with different Sb dopping contents. (a) 3 wt% Sb-doped WO_3. Inset is a digital photo that shows a light yellow color of the sample. (b) A close-up of one typical single crystal of 3 wt% Sb-doped sample. (c) 7 wt% Sb-doped WO_3. Inset is a digital photo that shows a simialr light yellow color of the sample. (d) A close-up of one typical single crystal of 7 wt% Sb-doped sample.

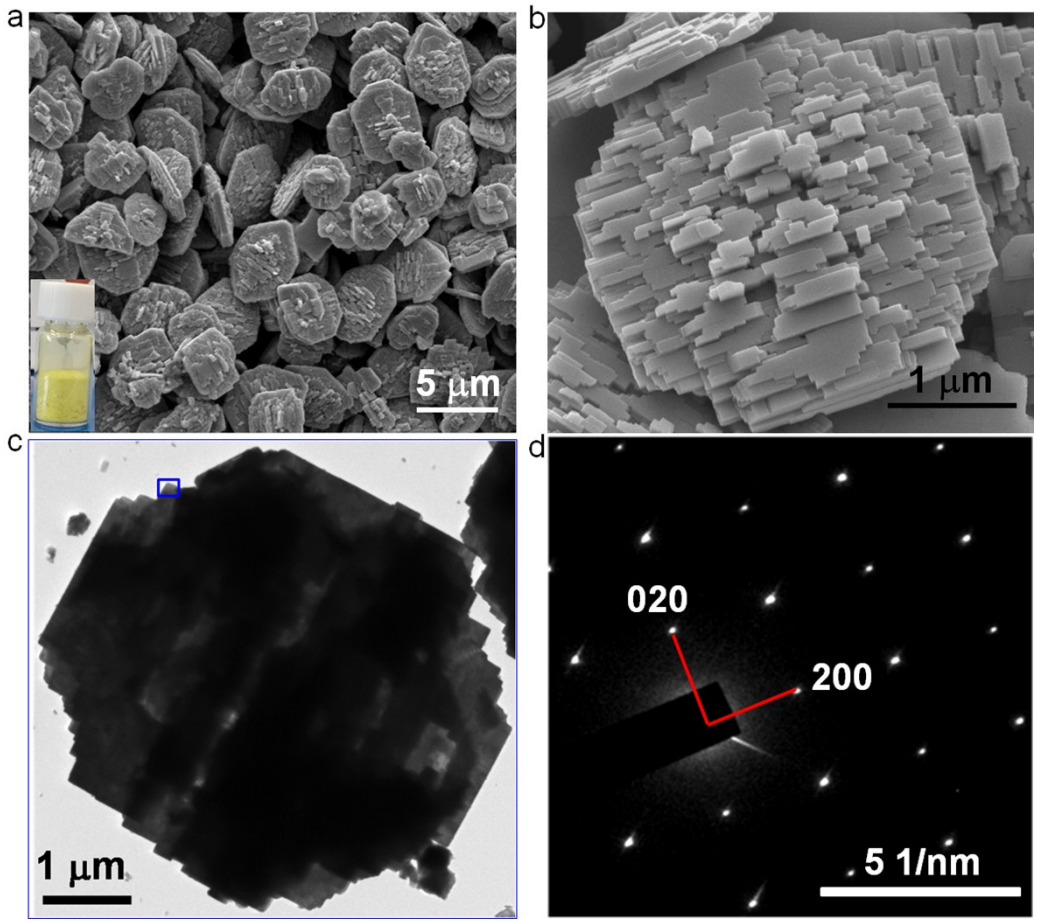

Fig. S4 ESEM and TEM images of 2D quasi-regular polygon WO_3 (QRPW) gas sensing material from urchin-like $W_{18}O_{49}$ nanocrystals with some nanowires. (a) ESEM image of a large-scale typical morphology of 2D QRPW. Inset is a digital photo that shows a yellow color of the sample. (b) The close-up image of one typical 2D QRPW. (c) TEM image of one typical 2D QRPW. (d) The SAED pattern of 2D QRPW in a blue square frame in figure c, indicating a single crystal structure.

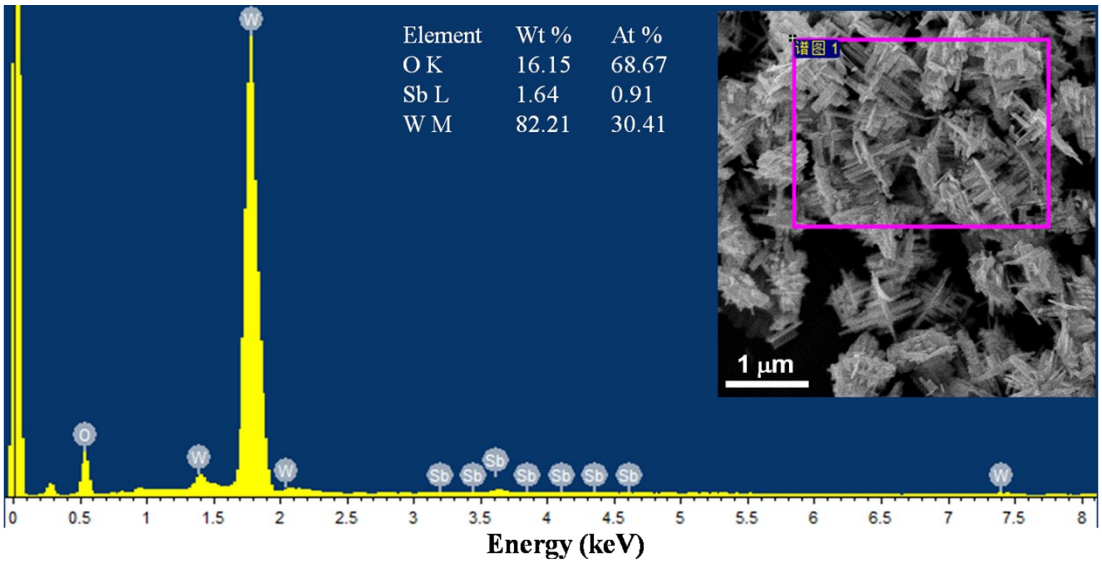

Fig. S5 EDS spectra of the 3D HMSW sample, indicating Sb ions doping successfully into WO_3 sample.

In order to further prove the existence of Sb-doped WO_3, energy dispersive spectrometer (EDS) was used to demonstrate the elemental composition of the 5.0 wt% Sb-doped WO_3. The peaks of the W, O and Sb elements are presented in the spectrum of Fig. S5. The concentration of Sb component is about 1.64 wt% corresponding to Sb doping concentration of 5.0 wt%, which is lower than that of doping in experimental procedure. The reason is that the two-step hydrothermal process may result in the loss of the antimony source in the reaction system.

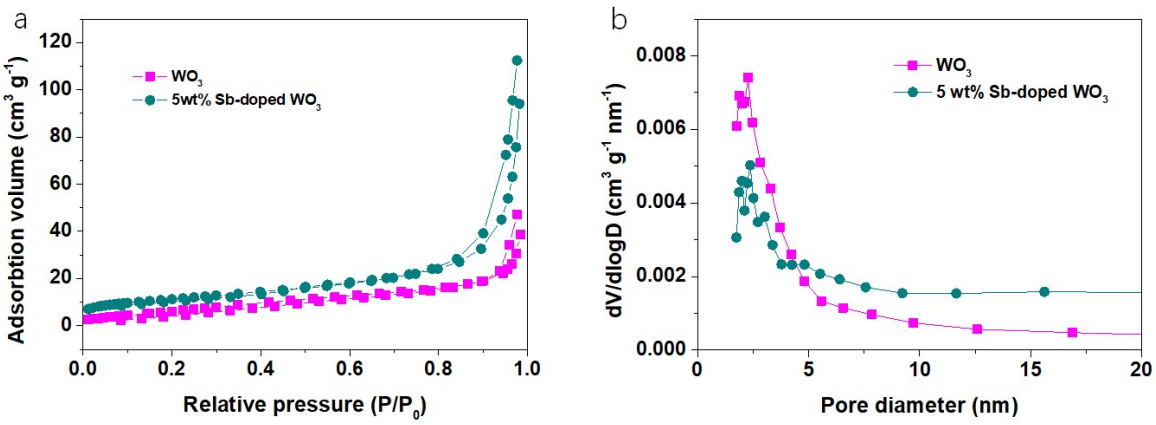

Fig. S6 The nitrogen adsorption analysis for the 2D QRPW (pure WO_3) and 3D

HMSW (5 wt% Sb-doped WO_3) samples obtained after carbonization in N_2 at 300 ºC. (a) Nitrogen adsorption-desorption isotherms. (b) The corresponding pore size distribution.

The nitrogen adsorption/desorption isotherms of the 2D QRPW (pure WO_3) and 3D HMSW (5 wt% Sb-doped WO_3) samples were recorded, as shown in Fig. S6. The isotherm for these samples is of type IV classification. Both pure WO_3 and Sb-doped WO_3 show similar isotherm curves, with sharp capillary cnodensation steps at a pressure (0.8-1.0), which suggests that mesopores are well develop in pure WO_3 and Sb-WO_3. Corresponding pore size distributions are observed (Fig. S6b). The pore size is estimated from the adsorption branch using the BJH method. The statatic size of small pores are about 2.5 nm. The small pores might produced from three-dimensionally ordered assembly of Sb-WO_3. These data the sepcific surface areas of these samples with the corresponding pore volumes and pore sizes are summarized in Table S2.

Consequently, highly efficient contact is exepcted between NO_2 and our 3D HMSW sample. An environment with concentrated NO_2 molecules on the 3D HMSW gas sensing material can speed up the diffusion and transport of target gas into the sensing layer and prompt the reaction between more adsorbed various oxygen ions (O_2^-, O^-) and NO_2 gas.

Table S2. Texture poperties of the 2D QRPW (pure WO_3) and 3D HMSW (5 wt% Sb-doped WO_3) samples and commercial WO_3 particles.

Sample	BET surface area ($m^2 g^{-1}$)	Total pore volume ($cm^3 g^{-1}$)	Average pore size (nm)[a]
2D QRPW (pure WO_3)	26.8	0.06	8.1
3D HMSW (Sb-doped WO_3)	40.0	0.14	16.7
Commercial WO_3 particles	6	/	/

a The pore sizes were derived from the adsorption branches of the isotherms by using the BJH method.

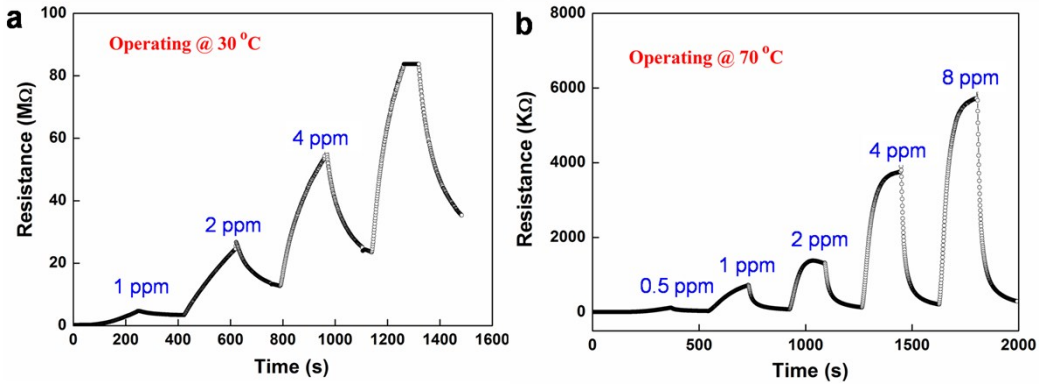

Fig. S7 For the HMSW sensor (5 wt% Sb doping), the transient resistance to 1-4 ppm NO_2 at the OT of 30 °C (a) and 70 °C (b) the transient resistance to 0.5-8 ppm NO_2, respectively.

The transient resistance with time of the 3D HMSW sensor to different concentration of NO_2 gas at 70 ºC was used to estimate the Sb doping effect on the type of the semiconductor, as shown in Fig. S7. The electrons are captured by NO_2

from conductance band owing to its unique electrophilic property to produce adsorbed $NO_2^-{}_{(ads)}$, resulting in the resistance of the semiconductor increases. Thus, the carriers of the n-type semiconductor are electrons. Owing to the definition of n-type semiconductor is that a type of extrinsic semiconductor where the doped atoms are capable of providing extra conduction electrons to the host materials. This creates an excess of negative (*n*-type) electron charge carriers. So, we surmise the 3D HMSW is still *n*-type semiconductor.

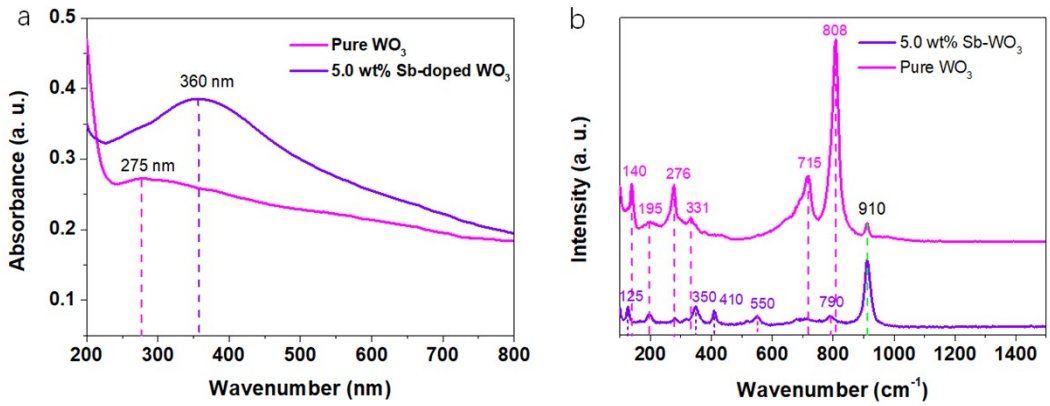

Fig. S8 Comparison of the UV-visible spectra (a) and Raman spectra (b) of the 2D QRPW (pure WO_3) and 3D HMSW (Sb-doped WO_3) samples.

As for the electronic effects, the research on the optical bandgap using a UV-Visible spectroscope is also needed. Figure S8a shows the absorptance spectra of pure WO_3 and Sb-doped WO_3. We found that, the characteristic adsorption peak positions shifted from about 275 nm in pure WO_3 to 360 nm in Sb-doped WO_3, which is nearly visible wavelength range, giving rise to the great red shift of characteristic absorption band. Therefore, we can infer that the Sb-doped WO_3 sample has a narrow band gap while pure WO_3 sample has a wide one. On the one hand, according to previous

reports,[6,7] defects could cause a decreased band gap, so the lower band gap of Sb-doped WO_3 may be attributed to its much more structural defects which is proved by XPS characterization and the first-principles total-energy calculation in main text (Fig. 5 and 6). The other reason for the narrow hand gap may be due to large density carriers occupying the lowest conduction band of the Sb-doped WO_3 sample. Some researchers [6,8,9] have reported that the decrease of the band gap could cause the increase of the gas sensing response, since the decreased band gap can produce more free electrons on the surface of sensing materials which will faciliate oxygen adsorbing, and then generate more adsorbed oxygen species which are beneficial for the sensing process.

As shown in Fig. S8b, the pure WO_3 sample exhibits typical Raman adsorption bands of 273, 327, 715, and 790 cm^{-1}, which are similar to those of the commercial WO_3 powder and can be identified as the four strong modes of WO_3.[10,11] The Raman bands at 273 and 327 cm^{-1} correspond to the O-W-O bending modes of bridging oxygen, and the bands at 715 and 790 cm^{-1} can be due to stretching modes. These are consistent with a monoclinic structural WO_3.[12]

Table S3. NO_2 gas sensing performance in our present work and those reported in the literatures. Concentrations (*C*, ppm), working temperature (*T*, °C), sensitivity (*S*), and year (reference [ref.]).

Materials	C	T	*S*	Year [ref.]
Cr-doped WO_3	1	230	7	2007 [13]
Au-doped WO_3	5	150	90	2008 [14]

WO_3 nanorods	10	200	209	2012 [15]
NiO/WO_3	10	25	3	2014 [16]
3D WO_3	10	110	20.5	2015 [17]
Fe-doped WO_3	12	150	105	2015 [18]
3DOM WO_3/Li	1	150	600	2016 [6]
Sb-doped WO_3	2	125	25	2017 [19]
3D HMSW (Sb-WO_3)	2	30	122	2018 (Present work)

References

1 J. Polleux, N. Pinna, M. Antonietti, M. Niederberger, *J. Am. Soc. Chem.*, 2005, **127**, 15595-15601.

2 A. Yella, M. N. Tahir, S. Meuer, R. Xentel, R. Berger, M. PanthÖfer, W. Tremel, *J. Am. Chem. Soc.*, 2008, **130**, 7780-7781.

3 K. Lee, W. S. Seo, J. T. Park, *J. Am. Soc. Chem.*, 2003, **125**, 3408-3409.

4 Y. Tian, S. Cong, W. Su, H. Chen, Q. Li, F. Geng, Z. Zhao, *Nano Lett.*, 2014, **14**, 2150-2156.

5 R. F. Garcia-Sanchez, T. Ahmido, D. Casimir, S. Baliga, P. Misra, *J. Phys. Chem. A*, 2013, **117**, 13825-13831.

6 Z. Wang, X. Fan, D. Han, F. Gu, *Nanoscale*, 2016, **8**, 10622-10631.

7 K. H. Lim, K. Kim, S. Kim, *Adv. Mater.*, 2013, **25**, 2994-3000.

8 Z. Wang, J. Xue, D. Han, F. Gu, *ACS Appl. Mater. Interfaces*, 2015, **7**, 308-317.

9 Y. R. Wang, B. Liu, S. H. Xiao, H. Li, L. L. Wang, D. P. Cai, D. D. Wang, Y. Liu, Q. H. Li, T. H. Wang, *J. Mater. Chem. A*, 2015, **3**, 1317-1324.

10 Y. H. Zhu, Y. Zhao, J. H. Ma, X. W. Cheng, J. Xie, P. C. Xu, H. Q. Liu, Y. H. Deng, D. Y. Zhao, *J. Am. Chem. Soc.*, 2017, **139**, 10365-10373.

11 L.Wang, A. Teleki, S. E. Pratsinis, P. I. Gouma, *Chem. Mater.*, 2008, **20**, 4794-4796.

12 L. Wang, Y. Wang, Y. Cheng, Z. Liu, Q. Guo, M. N. Ha, Z. Zhao, *J Mater. Chem. A*, 2016, **4**, 5314-5322.

13 E. Rossinyol, A. Prim, E. Pellicer, *Adv. Funct. Mater.*, 2007, **17**, 1801-1806.

14 H. Xia, Y. Wang, F. Kong, S. Wang, B. Zhu, X. Guo, J. Zhang, Y. Wang, S. Wu, *Sens. Actuators, B*, 2008, **134**, 133-139.

15 S. Bai, K. Zhang, R. Luo, D. Li, A. Chen, C. C. Liu, *J. Mater. Chem.*, 2012, **22**, 12643-12650.

16 M. Bao, Y. Chen, F. Li, J. Ma, T. Lv, Y. Tang, L. Chen, Z. Xu, T. Wang, *Nanoscale*, 2014, **6**, 4063-4066.

17 J. J. Qi, S. Gao, K. Chen, J. Yang, H. W. Zhao, L. Guo, S. H. Yang, *J. Mater. Chem. A*, 2015, **3**, 18019-18062.

18 T. Tesfamichael, C. Piloto, M. Arita, *Sens. Actuators B*, 2015, **221**, 393-400.

19 J. H. Sun, J. Guo, J. Y. Ye, B. J. Song, K. W. Zhang, S. L. Bai, R. X. Luo, D. Q. Li, A. F. Chen, *J. Alloy. Compd.* 2017, 876-884.